Single Metal Photodetectors Using Plasmonically-

Active Asymmetric Gold Nanostructures

Mahdiyeh Abbasi¹, Charlotte I. Evans^{2,†}, Liyang Chen³, and Douglas Natelson^{1,2,*}

¹Department of Electrical and Computer Engineering, Rice University, Houston, TX 77005,

USA

²Department of Physics and Astronomy, Rice University, Houston, TX 77005, USA

³Applied Physics Graduate Program, Rice University, Houston, TX 77005, USA

ABSTRACT

Plasmonic-based photodetectors are receiving increased attention because simple structural changes can make the photodetectors spectrally sensitive. In this study, asymmetric gold nanostructures are used as simple structures for photodetection *via* the photothermoelectric response. These single metal photodetectors use localized optical absorption from plasmon resonances of gold nanowires at desired wavelengths to generate temperature gradients. Combined with a geometry-dependent Seebeck coefficient, the result is a net electrical signal when the whole geometry is illuminated, with spectral sensitivity and polarization dependence from the plasmon resonances. We show experimental results and simulations of single-wavelength photodetectors

at two wavelengths in near IR range: 785 nm and 1060 nm. Based on simulation results and a model for the geometry-dependent Seebeck response, we demonstrate a photodetector structure that generates polarization-sensitive responses of opposite signs for the two wavelengths. The experimental photothermoelectric results are combined with simulations to infer the geometry dependence of the Seebeck response. These results can be used to increase the responsivity of these photodetectors further.

KEYWORDS plasmons, Seebeck coefficient, photothermoelectric effect, photodetector, gold nanowire

Plasmons are the collective oscillations of the incompressible electronic fluid in conductors, and often may be excited optically. The geometry of metallic nanostructures can be tuned so that localized surface plasmons (LSPs) are resonant at particular incident wavelengths and polarizations.[1,2]. This resonant coupling to light leads to enhanced scattering and absorption.

[3] Plasmon-induced heating is directly proportional to the imaginary part of the dielectric function of the metal.[4]

Optically driven heating can be used in conjunction with thermoelectric response to enable photodetection via the photothermoelectric (PTE) effect.[5] Charge carriers in a conductor heated under a temperature gradient tend to diffuse from high to low temperatures. In an open-circuit configuration, an internal electric field builds up to offset this diffusion, producing an open circuit voltage (the Seebeck effect), such that, locally, $\nabla V = -S \times \nabla T$ in which S is the Seebeck coefficient and ∇T is the temperature gradient. A traditional thermocouple can be made by

having two conductors with different S in contact with each other. When that junction is heated relative to the ends of the materials, the open circuit voltage is proportional to difference in S as well as the temperature gradient. The electronic contribution to the Seebeck coefficient S is often modeled by Mott's formula [6] $S = -\frac{\pi^2 k_B^2 T}{3e} \left(\frac{d \ln \sigma}{dE}\right)_{E=E_f}$. In this equation, σ is the energy-dependent electrical conductivity, k_B is the Boltzmann constant, T is temperature, e is the electron charge, E is the electron energy, and E_F is the Fermi energy of the conductor. The energy-dependent electrical conductivity is related to the scattering processes in the conductor. [7] When the conductor dimensions are comparable to the mean free path of carriers, the electrical conductivity and thus S can be manipulated by engineering the geometry. As a result, it is possible to make thermocouples with a single conductor. [8-11] Other factors that can tune the Seebeck coefficient include surface chemistry, [12] impurity concentration, [13] strain, [14,15] and modifications to band structure.

Photodetectors based on PTE do not require external bias, so their intrinsic noise source is mainly Johnson-Nyquist thermal noise.[5] PTE-based photodetectors have been put forward based on bolometric metal structures,[10,11,16] plasmonic metal structures coupled to semiconductor materials [17,18] and devices incorporating 2D materials.[19-22] In this study we demonstrate integrated photodetection structures combining the geometric spectral tunability and polarization sensitivity of LSPs, and the structural engineering of Seebeck response. We show experimental results and matching finite-element simulations for gold plasmon-resonant single-wavelength PTE detectors designed for 785 nm and 1064 nm incident wavelength. With this understanding and a model for geometric dependence of Seebeck response, we demonstrate a PTE-based single-metal structure that generates polarization-sensitive photovoltages of

opposite signs for the two wavelengths. The experimental response confirms the consistency of the assumed geometry dependence of the Seebeck coefficient.

RESULTS AND DISCUSSION

Figure 1a shows the experimental approach for measuring the steady-state PTE response, using a laser as the incident light source, with spot size tuned *via* the objective/sample distance. To be effective for unfocused photodetection applications, the net PTE response for a structure under flood (unfocused) illumination must be non-zero. In a single-metal structure symmetric about its midpoint (such as bow-tie constriction connected to two pads [14]), the temperature profile when uniformly illuminated and the Seebeck distribution are both spatially symmetric. This leads to a local PTE map acquired under focused illumination that is antisymmetric. This implies that when the whole geometry is uniformly illuminated, the net open circuit voltage would be zero and there would be no photodetection. An asymmetric geometry, conversely, in general has an asymmetric temperature profile when uniformly illuminated, as well as an asymmetric Seebeck distribution, so when the whole geometry is illuminated, the open-circuit voltage should be a non-zero value. In this work we create asymmetric structures to have a plasmonic resonance and hence enhanced absorption and elevated temperatures on one side, combined with a spatially asymmetric Seebeck distribution.

The LSP mode employed here is the dipolar transverse mode of a gold nanowire, excited when incident polarization is aligned transverse to the wire's long axis. For a wire with a fixed thickness, there will be wavelength-dependent width that resonantly couples to the optical source. We find the resonant width for a given incident wavelength by calculating the width dependence of the absorption of a nanowire using the finite element method (FEM) package

COMSOL Multiphysics. In these simulations, a plane wave with a transverse polarization is applied to a cross-section of a nanowire at certain width and thickness and the total integrated absorption power is calculated as a function of wire width. Absorption calculations for two wavelengths in near IR range are shown in Fig. 1b. In these simulations, the thickness of silicon oxide is 2 µm, the thickness of the nanowire is fixed at 18 nm, and the width of the gold nanowire varies from 50 nm to 1000 nm. Absorption plots for other gold thicknesses and silicon oxide thicknesses are shown in Fig. S1. The peaks in the absorption plots correspond to the transverse LSP resonant width at each wavelength. Based on these simulations, we can design an optimized photodetector for each of the wavelengths.

A single-wavelength photodetector device is shown in Fig. 1c. The nanowire in the middle of the device is tapered such that the wider side is plasmonically resonant for the designated wavelength (where the peak happens in the Fig. 1b plot), and the narrower side's width is farther away from the plasmonic resonance. Based on Fig. 1b, for detectors active at 1060 nm wavelength, the width of the wider side of the tapered nanowire is ~300 nm, and the narrower side's width is ~100 nm. For detectors active at 785 nm wavelength, the widths are ~170 nm and ~50 nm, respectively. By designing the wider side to be plasmonically resonant, the responsivity of the photodetectors at a single wavelength is much higher because of the enhanced absorption (*via* resonance and metal area) coupled with the spatial dependence of the Seebeck coefficient.

Modifications to the Mott formula (see SI) have been proposed that account for boundary scattering effects on the carrier mean free path.[14, 23] Based on this, when the wire width is not much larger than the carrier mean free path in the unbounded metal film, the narrower the nanowire, the smaller the Seebeck coefficient will be due to boundary scattering (assuming a positive *S*). Thus, from where the width suddenly decreases from the fan-outs to the wider side of

the nanowire, the local Seebeck coefficient drops suddenly ($S_1 < S_0$ in Fig. 1c). The Seebeck coefficient continuously decreases along the tapered nanowire ($S_2 < S_1$). Finally, the narrower side of the tapered wire connects to the fan-out and the Seebeck coefficient abruptly increases again ($S_0 > S_2$). The expected spatial dependence of the Seebeck coefficient of the device in Fig 1c is shown in Fig. 4a, showing a model (described below and in the SI) that the change in S is inversely proportional to the width of the nanowire.[23]

With one side of the device being connected to the ground and based on the Seebeck map, if the heat source is localized on the wider side junction (where S_0 changes to S_1 in Fig. 1c), the sign of the thermovoltage is the same as if the heat source is located in the middle of the device (where S_1 gradually changes to S_2). Conversely, the thermovoltage is of the opposite sign if the heat source is instead located on the narrower side junction (where S_2 changes to S_0). For higher responsivity for this plasmonically based photodetector, we need the sign of the Seebeck change on the tapered nanowire (and hence the sign of the PTE signal when heating is located on the nanowire) to be the same as the sign of the Seebeck change where the plasmonically resonant nanowire end joins the fanout (and hence the sign of the PTE signal when heating is located at that location).

The sign of the thermovoltage at the tapered nanowire is important for two reasons. First, the plasmonic resonances shown in Fig. 1b are comparatively broad, so that when one side of the nanowire has the transverse plasmon coupling resonantly with the optical source, the other widths across the tapered nanowire still contribute measurably even though they are off resonance. Second, when the laser is focused on the nanowire, the local temperature increases more than when the laser is closer to the fan-outs because the fan-outs have improved thermal conduction and behave as a heat sink. The simulation results of the temperature profile of a 1060 nm photodetector at two polarizations and different laser positions are shown in Fig. S5.

PTE maps for focused laser scans of two single-wavelength photodetectors designed for 1060 nm and 785 nm wavelengths are shown in Fig. 2. All of the open circuit voltage data are normalized to the incident power, helpful because of the linear optical power dependence of the PTE signals. The device that is presented in Fig. 2a and Fig. 2b is designed for 1060 nm incident wavelength. The top row of Fig. 2a shows the PTE map of the device when the laser has longitudinal polarization, and the bottom row shows the results when the incident laser has transverse polarization. Columns in Fig. 2a show the PTE map with different laser spot sizes (degrees of defocus). Fig. 2b shows the polarization dependence of the same device under flood illumination when the laser is expanded the most (spot size 43 µm as determined by knife edge) and the laser is positioned in the middle of the device. As shown in Fig. 2b, the response of the photodetectors is polarization dependent. Fig. 2c and Fig. 2d show the results for a different detector device designed for 785 nm incident wavelength. These results show that when the laser is expanded to approach flood illumination, the signal from the plasmonically resonant side dominates at transverse polarization. The responsivities of these devices are 11.3 $\frac{mV}{W}$ and 10.3 $\frac{mV}{W}$ for the single-metal devices in Fig. 2a and Fig. 2c, respectively, using the effective area inferred from simulations in COMSOL. See the SI.

We compare these sensitivities with other detector approaches. The responsivity of PTE photodetectors based on semiconductors can be as large as volts per watt.[5,19] Semiconductors have a higher Seebeck coefficient and smaller heat capacity compared to metals. The single-metal structures in this work have responsivity comparable to some graphene-based photodetectors [5,24] and have a comparatively simple (single-material) fabrication process, streamlining large-scale fabrication. Because of plasmonic resonances, such plasmonic PTE structures can harvest light over an area larger than their geometric size,[3] with polarization and wavelength selectivity.

While gold has comparatively poor Seebeck response, its structures are chemically stable and enable plasmon-based photodetection in the near IR range. Simulation results show that the responsivity of a metallic based photodetector comprising several thermocouples made by two different metals with high S difference can be as large as $112 \frac{mV}{W}$.[16] The fabrication process of a single metal photodetector is much easier. The response time of these detectors is set by the thermal timescales for the structures, and (see SI) is estimated to be slower than the photodetectors based on hot carriers [25,26] and faster than some photodetectors based on semiconductors.[5, 19]

It is possible to increase the responsivity of photodetectors presented here by fabricating several of them in parallel. Decreasing the thermal conductivity to the substrate also can increase the responsivity by increasing the temperature rise for a given incident optical power. Changing the substrate or decreasing the temperature of the environment [27] are possibilities to decrease the thermal conductivity to the substrate. For completeness, in the SI we show the response of the detector structures away from their designed wavelengths (Fig. S2, S3).

Based on the logic and approach above, it is possible to design a single photodetector that detects and discriminates two wavelengths. Fig. 1d shows the structure of a photodetector such that upper half of the device is plasmonically resonant at 1060 nm, and the bottom half is plasmonically resonant at 785 nm. The PTE results of this structure are shown in Fig. 3. Fig. 3a and Fig. 3b show the response of this structure at 1060 nm, and Fig. 3c and Fig. 3d show the response of this structure at 785 nm. The sign of the thermovoltage at the upper tapered nanowire is different from the sign of the signal on the bottom tapered nanowire because of the geometry and the resulting mirrored Seebeck coefficient change. As shown in Fig. 3, when the laser is maximally expanded with transverse polarization, the upper tapered nanowire dominates the sign

of the photovoltage signal at 1060 nm, while at 785 nm, the signal is dominated by the bottom tapered nanowire. The responsivity of this photodetector at 1060 nm is $5.15 \frac{mV}{W}$ and at 785 nm the responsivity is $7.10 \frac{mV}{W}$.

The reason that the responsivity of this device is smaller than the photodetectors designed solely for 785 nm or 1060 nm (Fig. 2) is that two opposite signs of the photovoltage at two tapered nanowires work against each other. This results in a net decrease of the impact of the plasmonically resonant side, compared to the single-wavelength-optimized detectors.

To improve this device's responsivity and to optimize this approach in general, we need to know quantitatively how much the Seebeck coefficient changes when metal wire widths change in these devices.

We were able to infer reasonable values for Seebeck coefficient spatial distributions from several single tapered devices based on the experimental PTE maps by comparison with simulations in COMSOL Multiphysics. The results are shown in Fig. 4. As described above, the narrower the metallic nanowire is, the smaller the Seebeck coefficient will be. Previous studies [23, 28] have shown that the Seebeck coefficient in thin films (with infinite width and length) is inversely proportional to the film thickness. In this study, first, we calculated the Seebeck coefficient for an Au film with 18 nm thickness and infinite width and length and then used a similar formula to account for the width change across the device (see SI). Fig. 4a shows the assumed Seebeck map across the length of the tapered nanowire. For extracting the Seebeck coefficient map of a tapered nanowire, the experimental PTE results when the laser is expanded and positioned in the middle of the device for two transverse and longitudinal polarizations are considered. The experimental photovoltage results when the focused laser scans the length of the

nanowire are also considered. First, temperature distributions are simulated in COMSOL Multiphysics for each case described above. Then, based on each case's experimental results, we converge to reasonable fit parameters for S for each device. Fig. 4b shows simulation fit results of the Seebeck coefficient versus the inverse width of the Au nanowire at the thickness of 18 nm. Points of each color correspond to one device. The error bars in Fig. 4b for the simulation fits are dominated by systematic uncertainties in the measurements. For example, the diameter of the focused 1060 nm laser is close to the length of the tapered nanowire (~3µm), and each pixel size in the PTE map is $0.5\mu m \times 0.5\mu m$, so a small shift in the PTE map can change the inferred PTE cross section (see Fig. S9). More importantly, while acquiring PTE maps, there is some variation in the focus of the laser spot, while the spot is always assumed to be its minimum size in the simulations. As a result, the simulated temperature profiles and calculated PTE differ from experiments when the laser focus is poor. In Fig. 4b, the red data points correspond to a measurement taken with a defocused laser, which clearly has poor consistency with the other data sets and the simple theoretical model of the width variation of S. The Seebeck coefficients in Fig. 4a and Fig. 4b are plotted relative to S_0 shown in Fig. 4a. The detailed steps of simulations for one of the devices and the error bars definitions are shown in the SI. These simulations give us a good insight into the Seebeck coefficient relation as a function of the width of a gold nanowire at fixed thickness. These fits are consistent with the results with previous studies, as shown in the SI.

CONCLUSION

Simple geometrical variation in gold nanowires can change the Seebeck coefficient as well as the plasmonic resonance behavior of gold nanostructures. Here, we combined these two traits to fabricate photodetectors with a single metal based on photothermoelectric effect. These wavelength-dependent and polarization-dependent photodetectors are simple to fabricate, and by understanding the system, it is possible to engineer and design a photodetector that can detect and discriminate two target wavelengths. Using knowledge of the mechanisms at work, the Seebeck coefficient variation *versus* width change of the nanowire at 18 nm thickness is extracted from experimental results using comparison to finite element method (FEM) simulations. We can further increase the responsivity of these devices by changing the thermal conductivity to the substrate and by optimizing the Seebeck map based on the Seebeck coefficient change *versus* width of the nanowire. For photodetectors in other operating wavelength ranges, other plasmonically metals can be used; for example, Al or Ag.

MATERIALS AND METHODS

The gold structures are made on a thermally oxidized silicon substrate with an oxide thickness of 2 µm. Gold has a strong plasmonic resonance in the near infrared (IR) and exhibits high chemical stability. Large gold pads are patterned on the substrate using photolithography and ebeam evaporation of 60 nm Au with a 5 nm Ti adhesion layer. The plasmonic structures with tapered gold nanowires are patterned by electron beam lithography using an Elionix e-beam writer followed by e-beam evaporation of 18 nm Au with 1 nm Ti adhesion layer and liftoff by acetone. A K&S 4526 wire bonder is used to electrically connect the large pads on the geometry to chip carrier using gold wires with 100 microns in diameter. A CW laser is used as a heat source to apply a temperature gradient to the metal structure. The measurement setup is shown in Fig. 1a. The laser is focused on the structure using a Zeiss Epiplan-Neofluar 50x objective with an NA of 0.55. The focus of the laser and hence the spot size on the device is controlled by moving the sample stage towards the objective using a Thorlabs MTS50 1D stage motor. The size of the expanded beam is measured using knife-edge measurement.[29] During scanning measurements, two Thorlabs DRV001 stepper motors control the 2D movement of the sample

stage in the plane perpendicular to laser direction and the integrated steady-state open circuit photovoltage signal of the entire device is measured at each spot in the stationary state to obtain the PTE maps. The feature sizes seen in the photothermoelectric (PTE) maps presented in Fig. 2 and Fig. 3 are set by a combination of optics (the laser spot size, the scanning pixel size) and the thermal properties that set the laser-induced temperature profiles (thermal conductivity of the metal and substrate; thermal boundary resistance between the metal and substrate; and environment temperature). In the PTE maps presented here, the pixel size is $0.5 \mu m \times 0.5 \mu m$. The smallest laser spot diameters in the present setup for the 1060 nm and 785 nm CW lasers are 3.5 μm and 2.7 μm , respectively.

The integrated open circuit voltage at a fixed position of heat source in a 1D model should be given by $V = -\int_0^l S(x,T)\nabla T(x)dx$; The Seebeck coefficient S(x,T) of a device is a function of position and temperature. $\nabla T(x)$ is the gradient of the temperature distribution along the length of the device (I). We also assume that the contacts of the device are held at identical fixed temperatures (the ambient temperature of the substrate). In the experiment the laser is positioned and the open circuit photovoltage is amplified by a voltage preamplifier and measured with a lock-in amplifier. The lock-in amplifier is locked to the frequency of a chopper that modulates the laser intensity incident on the sample at 263 Hz. This modulation period is much longer that the thermal timescales of the structures,[30] so that all the data are recorded in the steady state. The sample stage is raster-scanned in x and y directions and at each point, the integrated steady-state open-circuit photovoltage of the entire device is measured. PTE signal as a function of the laser position can be mapped out; examples of these PTE maps are shown in Fig. 2 and Fig. 3. The spatial resolution is limited by the laser spot size, assuming good thermal conductivity to the substrate. With the beam focused, local response can be mapped, while sufficiently defocusing

the beam allows characterization of the device photoresponse to flood illumination. All the measurements are done at room temperature and in ambient conditions.

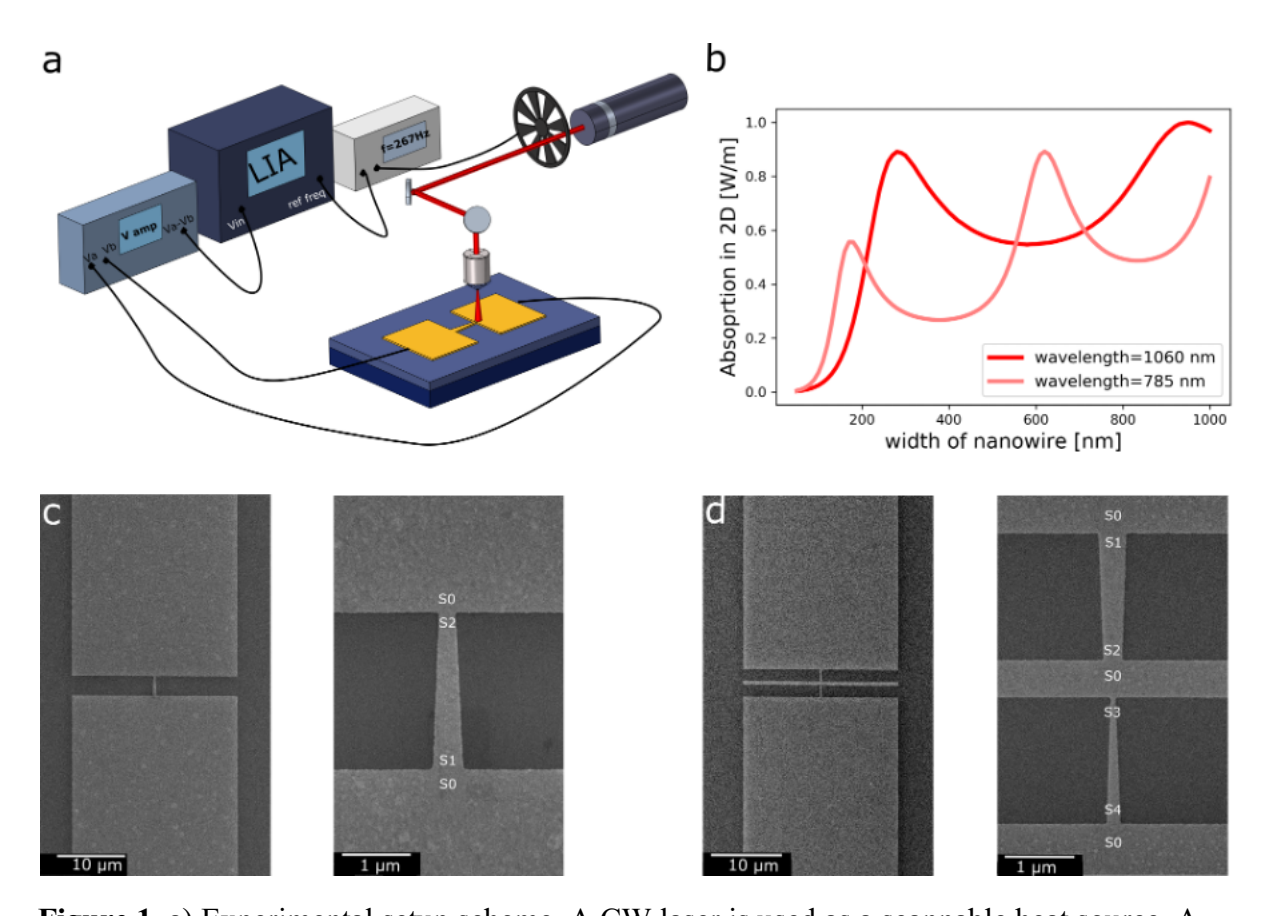


Figure 1. a) Experimental setup scheme. A CW laser is used as a scannable heat source. A chopper modulates the laser, and the open circuit voltage is measured using a lock-in-amplifier with its frequency locked to the chopper frequency. b) Calculated absorption as a function of wire width of a gold nanowire with a thickness of 18 nm for normal incidence and transverse polarization at two wavelengths, 1060 nm and 785 nm. The peaks correspond to plasmonic resonant absorption *via* transverse dipolar resonance. c) SEM images of the geometry of a single wavelength photodetector. d) SEM images of a double wavelength photodetector.

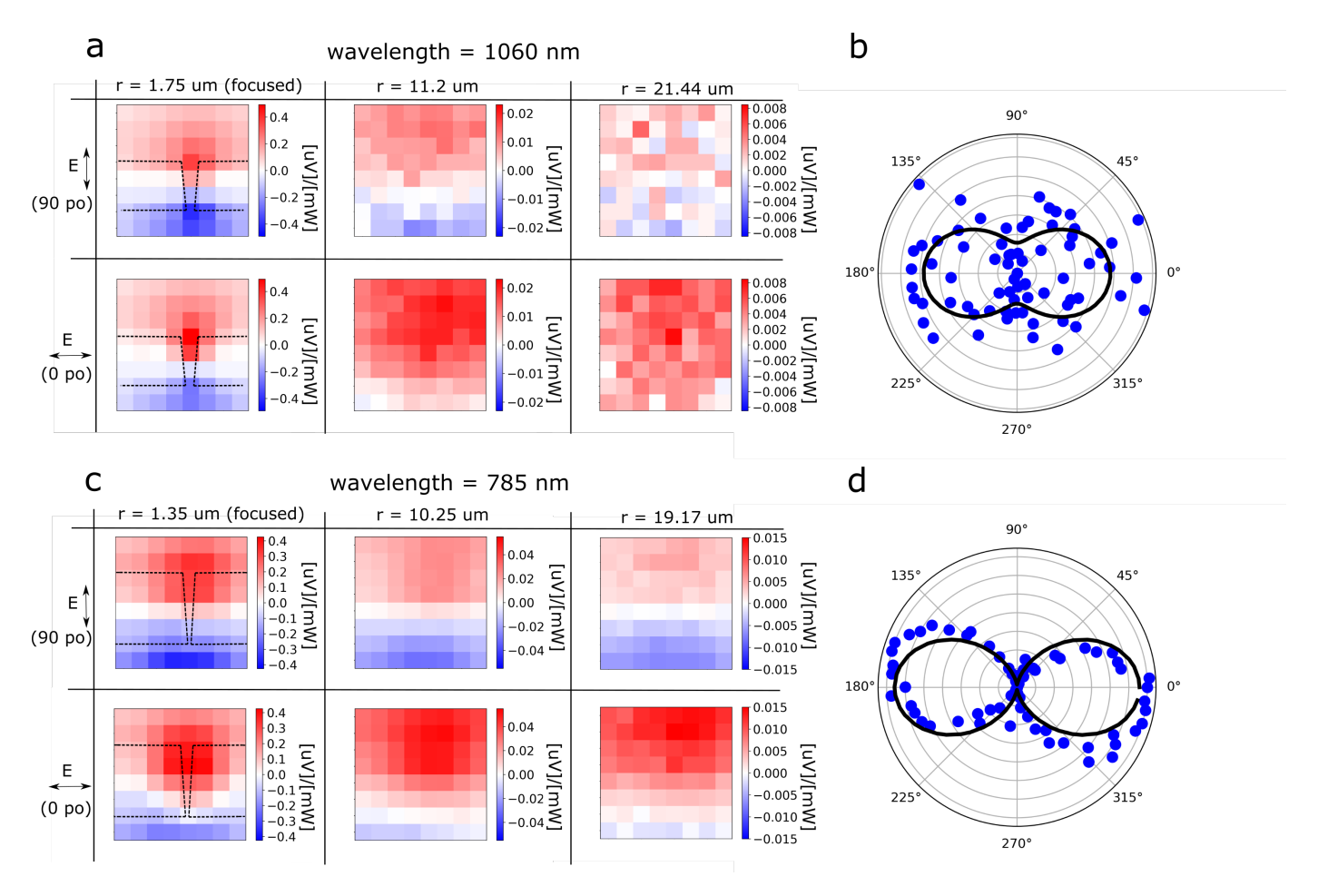


Figure 2. Single wavelength photodetector PTE results. a) PTE maps for a photodetector designed for 1060 nm wavelength. Tapered nanowire end widths are 300 nm and 100 nm. All PTE maps are taken over the same spatial area of the device. Each pixel size is $0.5 \,\mu\text{m} \times 0.5 \,\mu\text{m}$. The first row shows the longitudinal polarization results for different laser spot diameters $(2 \times r)$. The second row shows the transverse polarization results for different laser spot diameters. The parameter r is the radius of the laser spot hitting the surface of the sample. b) Polarization plot of the device shown in Fig. 1a. The laser is expanded with a diameter of 43 μ m, and the laser is positioned in the middle of the device. The black line shows the $(A \times cos^2 \theta + B)$ fit result. c) PTE map for photodetector designed for 785 nm wavelength. Tapered nanowire end widths are

200 nm and 50 nm. All maps are taken over the same spatial area of the device. Each pixel size is $0.5 \, \mu \text{m} \times 0.5 \, \mu \text{m}$. The first row shows the longitudinal polarization results for different laser spot diameters $(2 \times r)$. The second row shows the transverse polarization results for different laser spot diameters. The parameter r is the radius of the laser spot hitting the surface of the sample. d) Polarization map from the device shown in Fig. 1c. The laser is expanded with a diameter of $38.34 \, \mu \text{m}$, and the laser is positioned in the middle of the device. The black line shows the $(A \times cos^2 \, \theta + B)$ fit result.

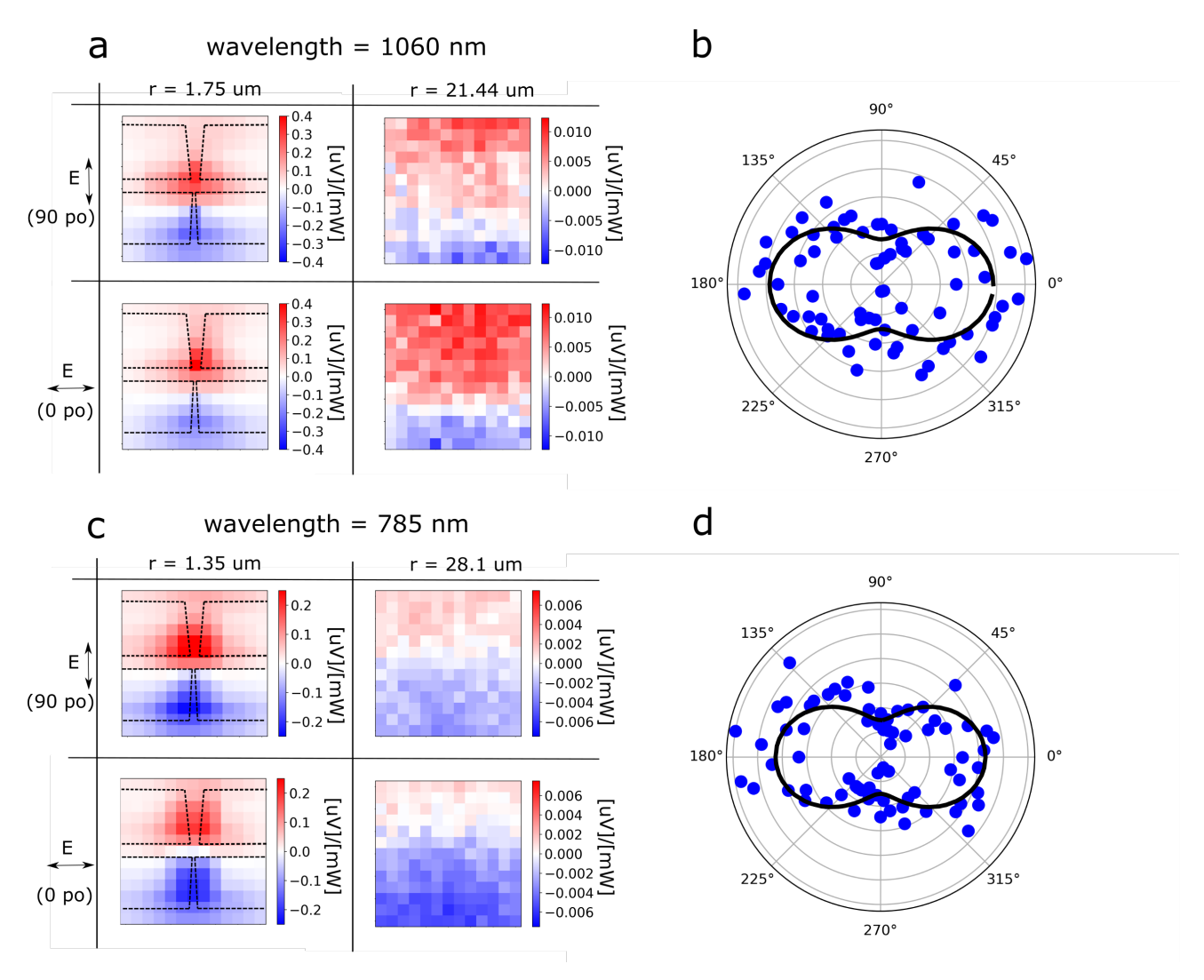


Figure 3. PTE results for a photodetector designed to respond to both 1060 nm and 785 nm wavelengths, but with opposite signs of signal. SEM image of this structure is shown in Fig. 1d. The tapered nanowire widths are 400 nm and 260 nm for 1060 nm side and 185 nm and 50 nm for 785 nm side. a) PTE map of the device when the 1060 nm CW laser is used as a heat source. The first row shows the PTE map for longitudinal polarization for focused and expanded laser. The second row shows the PTE map for transverse polarization. Each pixel size is

0.5 μ m×0.5 μ m. As is evident that when the laser is expanded, the positive signal is dominating the PTE map at transverse polarization, which corresponds to the resonant plasmon response at 1060 nm. The parameter r is the radius of the laser spot hitting the surface of the sample. b) polarization plot of the device shown in Fig. 3a. while laser diameter is 43 μ m and positioned in the middle of the device. The black line shows the (A × $\cos^2 \theta$ + B) fit result. c) PTE map of the same device when a 785 nm CW laser is used as a heat source. In this case, when the laser is expanded, the negative signal is dominating the signal at transverse polarization, which corresponds to the transverse resonance of plasmons at 785 nm. d) polarization plot of the same device when the 785 nm laser diameter is 56.2 μ m and positioned in the middle of the device. The black line shows the (A × $\cos^2 \theta$ + B) fit result.

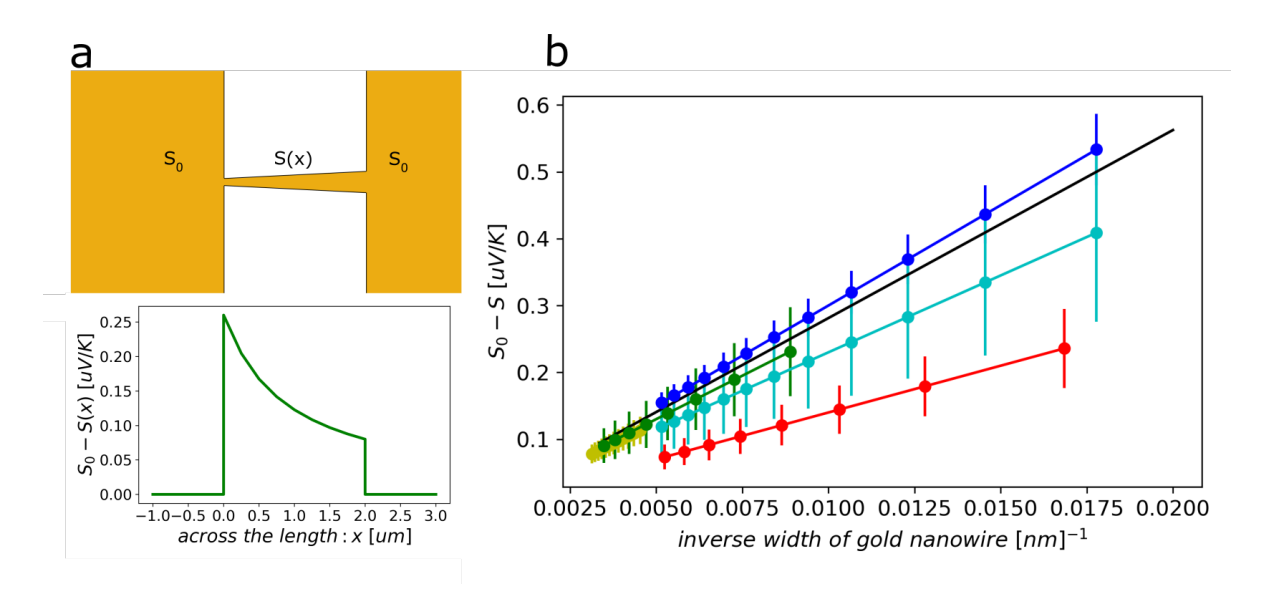


Figure 4. Simulation results of the Seebeck coefficient *vs.* width of the gold nanowire. a) Seebeck coefficient map across the length of the tapered nanowire. Local deviation of Seebeck coefficient from bulk value is assumed to be proportional to the inverse of the width of the nanowire (see the SI). b) Results of the simulation fits of Seebeck coefficient *vs.* inverse width of the gold nanowires with a thickness of 18 nm for five different devices. Each color represents a particular device. The black line represents the theory expectation (see SI). The red and light blue plots correspond to a measurement with a defocused laser.

ASSOCIATED CONTENT

Supporting Information. There is a pdf file of supporting information containing: a discussion of the effects of boundary scattering on the Seebeck coefficient; finite-element simulations of the

photodetector structures including temperature profiles under different illumination conditions; measurement of the laser spot diameter; and comparisons of results with different models for geometry-dependent Seebeck response. The following file is available free of charge.

AUTHOR INFORMATION

Corresponding Author

*Douglas Natelson (<u>natelson@rice.edu</u>)

Present Addresses

†Sandia National Laboratory, Sandia, NM 87185, USA.

Author Contributions

MA performed the experiments and simulations and analyzed the data. MA and CIE worked on the experimental setup and data acquisition. LC and MA measured the thermal noise. MA and DN wrote the manuscript. All authors have given approval to the final version of the manuscript.

ACKNOWLEDGMENT

M.A and D.N acknowledge Prof. Peter Nordlander and Prof. Longji Cui for useful discussions. D.N. and C.I.E. acknowledge Robert A. Welch Foundation award C-1636. D.N. and M.A. acknowledge support from NSF ECCS-1704625. LC and the noise measurement equipment were supported by DOE BES award DE-FG02-06ER46337.

REFERENCES

- 1. Lee, K.; Lin, S.; Lin, C.; Tsai, Yu. Size Effect of Ag Nanoparticles on Surface Plasmon Resonance. *Surface and Coating Technology* **2008**, *202*, 5339-5342.
- 2. Hao, F.; Nehl, C. L.; Hafner, J. H.; Nordlander, P. Plasmon Resonances of Gold Nanostar.

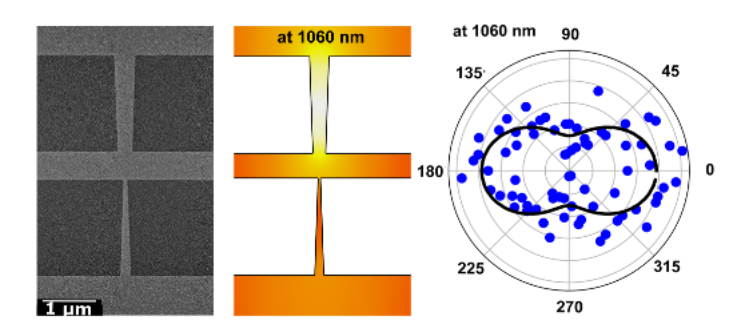
 Nano Lett. 2007, 7, 729-732.
- 3. Bohren, C. F. How Can a Particle Absorb More Than the Light Incident on It? Am. J. Phys. **1983**, *51*, 323-327.
- 4. Willets, K. A.; Van Duyne, R. P. Localized Surface Plasmon Resonance Spectroscopy and Sensing. *Ann. Rev. Phys. Chem.* **2007**, *58*, 267-297.
- 5. Lu, X.; Sun, L.; Jiang, P.; Bao, X. Progress of Photodetectors Based on the Photothermoelectric Effect. *Adv. Mater.* **2019**, *31*, 1902044.
- 6. Mott, N. F.; Jones, H. The Theory of the Properties of Metals and Alloys. Dover: New York, 1958.
- 7. Herzog, J. B.; Knight, M. W.; Natelson, D. Thermoplasmonics: Quantifying Plasmonic Heating in Single Nanowires, Nano Lett. **2014**, *14*, 499-503.
- 8. Szakmany, G. P.; Orlov, A. O.; Bernstein, G. H.; Porod. W. Single-Metal Nanoscale Thermocouples. IEEE Trans. Nano. **2014**, *13*, 1234-1239.
- 9. Sun, W.; Liu. H.; Gong, W.; Peng, L.; Xu, S. Unexpected Size Effect in the Thermopower of Thin-Film Stripes, J. Appl. Phys. **2011**, *110*, 083709.

- Szakmany, G. P.; Orlov, A. O.; Bernestein, G. H.; Porod, W. Novel Nanoscale Single-Metal Polarization Sensitive Infrared Detectors. IEEE Trans. Nano. 2015, 14, 379-383.
- 11. Szakmany, G. P.; Orlov, A. O.; Bernstein, G. H.; Porod, W, Shape Engineering of Antennacoupled Single-Metal Nanothermocouples. Infrared Phys. & Tech. **2015**, *72*, 101-105.
- 12. Wang, X.; Evans, C. I.; Natelson, D. Photothermoelectric Detection of Gold Oxide Nonthermal Decomposition. Nano Lett. **2018**, *18*, 6557-6562.
- 13. Otter, F. A. Thermoelectric Power and Electrical Resistivity of Dilute Alloys of Mn, Pd, and Pt in Cu, Ag, and Au. J. Appl. Phys. **1956**, *27*, 197-200.
- 14. Zolotavin, P.; Evans, C. I.; Natelson, D., Substantial Local Variation of the Seebeck Coefficient in Gold Nanowires. Nanoscale **2017**, *9*, 9160-9166.
- 15. Evans, Charlotte I.; Yang, Rui; Gan, Lucia T.; Abbasi, Mahdiyeh; Wang, Xifan; Traylor, Rachel; Fan, Jonathan A.; Natelson, Douglas. Thermoelectric Response from Grain Boundaries and Lattice Distortions in Crystalline Gold Devices, Proc. Nat. Acad. Sci. US 2020, 117, 23350-23355.
- 16. Briones, E.; Cuadrado, A.; Briones, J.; Diaz de Leon, R.; Martinez-Anton, J. C.; McMurty, S.; Hehn, M.; Montaigne, F.; Alda, J.; Gonzalez, F. J. Seebeck Nanoantennas for the Detection and Characterization of Infrared Radiation. Opt. Express 2014, 22, A1538-A1546.
- 17. Mauser, K. W.; Kim, S.; Mitrovic, S.; Fleischman, D.; Pala, R.; Schwab, K. C.; Atwater, H. A. Resonant Thermoelectric Nanophotonics. Nat. Nano. **2017**, *12*, 770-775.

- 18. Liu, W.; Wang, W.; Guan, Z.; Xu, H. A Plasmon Modulated Photothermoelectric Photodetector in Silicon Nanostripes. Nanoscale **2019**, *11*, 4918-4924.
- 19. Hsu, A. L.; Herring, P. K.; Gabor, N. M.; Ha, S.; Shin, Y. C.; Song, Y.; Chin, M.; Dubey, M.; Chandrakasan, A. P.; Kong, J.; Jarillo-Herrero, P.; Palacios, T. Graphene-Based Thermopile for Thermal Imaging Applications. Nano Lett. **2015**, *15*, 7211-7216.
- 20. Buscema, M.; Barkelid, M.; Zwiller, V.; van der Zant, H. S. J.; Steele, G. A.; Castellanos-Gomez, A. Large and Tunable Photothermoelectric Effect in Single-Layer MoS₂. Nano Lett. **2013**, *13*, 358-363.
- 21. Cai, X.; Sushkov, A. B.; Suess, R. J.; Jadidi, M. M.; Jenkins, G. S.; Nyakiti, L. O.; Myers-Ward, R. L.; Li, S.; Yan, J.; Gaskill, D. K.; Murphy, T. E.; Drew, H. D.; Fuhrer, M. S. Sensitive Room-Temperature Terahertz Detection *via* the Photothermoelectric Effect in Graphene. Nat. Nano. 2014, 9, 814-819.
- 22. Echtermeyer, T. J.; Nene, P. S.; Trushin, M.; Gorbachev, R. V.; Eiden, A. L.; Milana, S.; Sun, Z.; Schliemann, J.; Lidorikis, E.; Novoselov, K. S.; Ferrari, A. C. Photothermoelectric and Photoelectric Contributions to Light Detection in Metal-Graphene-Metal Photodetectors. Nano Lett. 2014, 14, 3733-3742.
- 23. Cattani, M.; Salvadori, M. C.; Vaz, A. R.; Teixerira, F. S. Thermoelectric Power in Very Thin Film Thermocouples: Quantum Size Effect. J. Appl. Phys. **2006**, *100*, 114905.
- 24. Chen, M.; Wang, Y.; Wen, J.; Chen, H.; Ma, W.; Fan, F.; Huang, Y.; Zhao, Z. Annealing Temperature-Dependent Terahertz Thermal-Electrical Conversion Characteristics of Three-Dimensional Microporous Graphene. ACS Appl. Mater. Interf. 2019, 11, 6411-6420.

- 25. Sun, D.; Aivazian, G.; Jones, A. M.; Ross, J. S.; Yao, W.; Cobden, D.; Xu, X. Ultrafast Hot-Carrier-Dominated Photocurrent in Graphene. Nat. Nano. **2012**, *7*, 114-118.
- 26. Tielrooij, K. J.; Massicotte, M.; Piatkowski, L.; Woessner, A.; Ma, Q.; Jarillo-Herrero, P.; Van Hulst, N. F.; Koppens, F. H. L. Hot-Carrier Photocurrent Effects at Graphene-Metal Interfaces. J. Phys.: Condens. Matt. 2015, 27, 164207.
- 27. Zolotavin, P.; Alabastri, A.; Nordlander, P.; Natelson, D. Plasmonic Heating in Au Nanowires at Low Temperatures: The Role of Thermal Boundary Resistance. ACS Nano 2016, 10, 6972-6979.
- 28. Das, V. D.; Soundararajan, N. Size and Temperature Effects on the Seebeck Coefficient of Thin Bismuth Films. Phys. Rev. B **1987**, *35*.12, 5990-5996.
- 29. Gonzalez-Cardel, M.; Arguijo, P.; Diaz-Uribe, R. Gaussian Beam Radius Measurement with a Knife-Edge: A Polynomial Approximation to the Inverse Error Function. Appl. Optics **2013**, *52*, 3849-3855.
- 30. Benner, D.; Boneberg, J.; Nürnberger, P.; Waitz, R.; Leiderer, P.; Scheer, E., Lateral and Temporal Dependence of the Transport through an Atomic Gold Contact under Light Irradiation: Signature of Propagating Surface Plasmon Polaritons. Nano Lett. **2014**, *14*, 5218-5223.

For Table of Contents Only



Supplementary Information: Single Metal

Photodetectors Using Plasmonically- Active

Asymmetric Gold Nanostructures

Mahdiyeh Abbasi¹, Charlotte I. Evans², Liyang Chen³, and Douglas Natelson^{1,2}

¹Department of Electrical and Computer Engineering, Rice University, Houston, TX 77005, USA

²Department of Physics and Astronomy, Rice University, Houston, TX 77005, USA

³Applied Physics Graduate Program, Rice University, Houston, TX 77005, USA

1. Modified Seebeck coefficient formula:

The Seebeck coefficient change in a thin film when the thickness is larger than the mean free path of the bulk can be written as:[S1]

$$\Delta S_{\rm F} = S_{\rm bulk} - S_{\rm F} = S_{\rm bulk} \frac{U}{U+1} \times \frac{3l}{8(1-p)t}$$

2. Simulations:

Simulations are done in COMSOL Multiphysics versions 5.4. The absorption plots shown in Fig. 1 is implemented in 2D using Electromagnetic wave physics (ewfd) in COMSOL. A plane wave with transverse polarization is applied to the cross-section of a gold nanowire. The geometry is shown Fig. S1a. The total absorption plots in Fig. 1 and Fig. S1 are the integral of the dissipated power across the area of the nanowire cross-section. The simulation is done in different widths, wavelengths, Au thickness, SiO₂ thickness, and with and without adhesion layer to calculate what is shown in Fig. 1 and Fig. S1.

The PTE signal simulations are implemented using Joule Heating physics in the software. Joule heating physics in COMSOL consist of Heating Transfer in Solids (ht) and Electric Currents (ec). The geometries in each simulation match with an actual device represented in. In the Electric Current physics (ec), one end of the metallic structure is defined to have zero voltage. Open circuit voltage is probed from the other end of the metallic structure. In Heating Transfer in Solids Physics (ht), the temperatures at two ends of the nanowire are forced to be at room temperature. Also, the bottom of the structure is fixed to room temperature, behaving as a heat sink. In Heating Transfer in Solids Physics (ht), a temperature profile is applied to the surface of the gold structure. This temperature profile is the result of another Multiphysics simulations where Electromagnetic wave physics(ewfd) and Heat Transfer in Solid(ht) are calculated. In Electromagnetic wave physics, a Gaussian beam source with the same full width at half maximum (FWHM) and power as the focused laser beam in the experiment is applied to the surface of the structure. The dissipated power in gold structure is calculated in Electromagnetic wave physics and it is passed to Heat Transfer Solid (ht) physics as the heat source and temperature profile can be simulated. Fig. S5 shows the simulation results where the temperature is calculated using Electromagnetic wave physics and Heat Transfer physics. Fig. S6 shows the Joule Heating simulation scheme where the temperature is imported from ewfd and ht simulations and the open circuit voltage is calculated.

For calculating the fits in Fig. 4, first, we simulated the temperature profile across the device when laser is focused and scans the length of the nanowire with 0.5 µm steps (same as the pixel size in PTE maps in experiments). We also simulated the temperature profile when the laser is expanded and positioned in the middle of the device at two polarization. The *T* profile simulations for a photodetector at 1060 nm are shown in Fig. S5. Later, we simulated the open circuit voltage at each laser position and each polarization by using the calculated T profiles. We assumed the

difference in local Seebeck coefficient across the device to be α/w where α is a constant and w(x) is the width across the tapered nanowire. We found the α that causes minimum deviation between PTE signal from simulation and experiment; In the case of applying a focused laser, first, the photovoltage signals across the length of the nanowire from the experiment and simulation are normalized to the maximum value from the experiment. This process is done for both polarizations. Then the square root of the sum of the square of the differences between simulation and experiment is calculated. The same process is done for the case when the expanded laser with transverse polarization is positioned in the middle of the device (for the expanded laser with longitudinal polarization, the signal amplitude is too small; Fig. 2a). The α corresponding to the minimum value for the sum of errors is recorded as the where the filled points are in Fig. 4. When the error is increased by 30%, the corresponding α is recorded as the top and bottom value of the error bars in Fig. 4.

The dash lines in Fig. S8 show the PTE signal along the cut-through direction along the length of the tapered nanowire, and the blue plots in Fig. S8 are the cut-through signals across the length of the nanowire from the experiment. The cut-through simulated results for two polarization for a photodetector designed for 785 nm is shown in Fig. S8 in pink. Later, the results are plotted as the Seebeck coefficient vs. the inversed width of the nanowire that is shown in Fig. 4b. The error bars for the simulation fits are dominated by systematic uncertainties in the experiment. As explained in the main text, the diameter of the focused laser on each device in the experiment might not be exactly the same size, but in the simulations, the focused laser has a fixed size. Each pixel size in PTE maps is $0.5 \mu m$ by $0.5 \mu m$ and the focused laser diameters for $1060 \mu m$ and $785 \mu m$ lasers are $3.5 \mu m$ and $2.7 \mu m$, respectively. (For information about the laser size measurements see the "laser diameter measurement" section in the SI). Both diameters are larger than the widths of the tapered

nanowires. This causes a little shift to the cut-through plots when the window of the PTE map shifts for less than 0.5 μ m. For example, the cut-throughs for two consecutive measurements are shown in Fig. S9. Here, the window in the second measurement is shifted by 0.3 μ m in x and in the y-direction. The shifts in these cut-throughs are obvious. Also, the fabricated devices might not have perfect edges across the length of them. Imperfections can randomly change the scattering pattern across the length of the device and change the Seebeck coefficient based on the discussion in the introduction of the main text. The blue plot in this figure corresponds to the device described in Fig. S8. In these simulations, S_0 is assumed to be 1.5 $\frac{\mu V}{K}$, which is the absolute Seebeck coefficient of gold,[S2] but this number does not change the PTE result simulations, as the open circuit voltage depends on relative Seebeck coefficients.

For optical simulations, the maximum mesh size for each domain is the effective wavelength in that domain divided by 5 ($\lambda/n/5$, where n is the index of refraction). Maximum mesh size for the gold film is smaller than the skin depth of the gold film in applied wavelength. For the thermal and electrical simulation, a coarser mesh is sufficient. For those simulations, the maximum element size in the gold film is the gold film thickness and in other areas is 1μ m.

For optical simulations, the real and imaginary parts of the permittivity are concerned. The permittivity parameters are extracted from the literature.[S5,S6,S7] For thermal simulations, the thermal conductivity, density, heat capacity at constant pressure are concerned. The parameters are used from the COMSOL library. For electrical simulations, the electrical conductivity and the Seebeck coefficients are used. The value for the conductivity is used from the COMSOL library. The value for the Seebeck coefficient of gold is taken from literature.[S2] Note that the relative

Seebeck coefficient in the simulation affects the open circuit voltage and not the absolute value of the Seebeck coefficient of each material.

3. Response time of these photodetectors:

COMSOL simulations of the PTE response have three steps: 1- wave optics simulations in a frequency domain where the light-matter interaction is simulated and the losses in the gold film is calculated. 2- heat transfer in a stationary state where the heat source comes from the losses calculated in the previous step and the temperature profile across the device is calculated. 3- joule heating where the temperature profile comes from the previous step and the open circuit voltage based on the Seebeck coefficients across the device is calculated. Time dependent simulations for the second and third steps can give us a good estimation of the response time of these photodetectors. The results are shown in Fig. S10, where it shows a response time of around 8 microseconds.

4. Laser diameter measurement:

The focused laser diameter is measured using the laser's white light image on the CCD. The edge of the laser beam is positioned on the edge of a gold film. Then, the sample stage moves in one direction using a Thorlabs BCS102 motor controller and Thorlabs DRV001 stepper motor with step sizes of 0.1 microns until the laser is passed from the edge. Laser diameter is the same size as the stage movement. The expanded laser diameter is measured by the knife-edge measurement. [S8] The knife-edge here is a razor blade. The razor blade is moved farther and closer to the objective focus point by a Thorlabs MTS50 1D stage motor and a Thorlabs KDC101 motor

controller. A Thorlabs MTS25 1D stage motor is used to move the razor blade from one side to the other to block the laser. A PM100D Thorlabs power meter is used to measure the fraction of the laser power that is not blocked with the razor. The results of the knife-edge measurements are shown in Fig. S4. Based on these results, the laser diameter change *vs.* change of distance from the objective is calculated by a linear fit through all the experimental results. The laser diameter at each distance from the objective focus point can be calculated by having the focused laser size and the knife-edge measurement results.

5. Noise of the devices and measurement:

To find the thermal noise of the detector, the sample was mounted on a custom low-frequency measurement probe and inserted into a cryostat (Quantum Design PPMS) with temperature stability better than 0.02% in the relevant temperature range. The measurement wirings are twisted pairs to reduce magnetic field induced noise. The sample, transmission lines, and the first pair of pre-amplifiers are shielded by a Faraday cage to reduce environmental noise. The voltage noise in the device is collected by two separate amplifier chains, each consisting of two preamplifiers (NF LI-75 and Stanford Research SR560, each with gain of 100). The two amplified signals are recorded by a high-speed data acquisition system (Picoscope 4262). Each time series containing 2,000,000 data points is taken with a sampling rate of 10 MHz. The two voltage time series are cross-correlated, revealing the true sample noise since the amplifier noise is nominally uncorrelated between the chains. We measured the Johnson noise at five temperatures around room T; 292.5-294.5 K. This is a relevant temperature range, as the simulation results show that while using an expanded laser with transverse polarization, T goes up by ~1 K; Fig. S5. The results of the noise measurements are shown in Fig. S11a. The results

match well with the theoretically expected value for our device with ~115 ohm resistance. $(4k_BTR=1.84\times10^{-18}\,[V^2/Hz])$. The thermal noise is measured 15 times at each temperature point. The vertical lines in Fig. S11a show the standard deviation of the thermal noise measurements at each temperature. Thus, the minimal noise theoretically possible in the detector operated at room temperature is about $1.35\times10^{-9}\,V/Hz^{1/2}$.

To measure the noise of the unoptimized measurement system, the PTE map of the same device has been acquired with the laser being completely blocked. The chopper is still on and the lockin amplifier's reference frequency is locked to the chopper frequency. The bandwidth of the lockin amplifier with the time constant of 200 ms and the output filter slope of 12 dB/Oct is 0.84 Hz. An example of the measured noise as a function of mapping position in this case is shown in Fig. S11b. As shown here and in four successive identical mapping runs with the laser off, the maximum noise amplitude of the PTE signal, is $\sim 30 \, \frac{\text{nV}}{\sqrt{\text{Hz}}}$.

This significantly exceeds the theoretical limit of the detector thermal noise. The measurement setup noise floor may be improved through the use of a voltage preamplifier optimized for the detector impedance. At our measurement frequency and at room T, the present voltage amplifier (Stanford SR560) has a minimum noise for a resistance as large as $100 \text{ k}\Omega$. The low resistance of our devices, $\sim 120 \Omega$, increases the noise of the preamplifier.

6. Effective area

For calculating the effective area, the field enhancement when the optical source is applied to the structure is simulated. In these simulations, an incident plane wave with the same intensity as the

expanded Gaussian beam is applied to the photodetector to optimize between the accuracy and the computational power. The polarization of the laser is transverse to excite plasmon modes that are the basis of these photodetectors. The intensity of the optical source matches the experiment. The area that encloses 35% of the maximum field enhancement and above is defined as the effective area, which is an estimation for 90% of the response area defined in Ref. S7. Fig. S12 shows the effective area for each of the photodetector described in the main text. Simulations show that the effective areas for the devices presented in Fig. 2a and Fig. 2c are $0.424~\mu m^2$ and $0.265~\mu m^2$, respectively. The effective area of the device presented in Fig. 3 differs at different wavelength. At 785 nm, the effective area is $0.393~\mu m^2$ and at 1060~nm, the effective area is $0.863~\mu m^2$.

7. Calculating the detectivity

Calculating the detectivity: The effective area and the noise results of these photodetectors are used to calculate the detectivity. In the following equations, D*, A, and NEP are detectivity, effective area, and noise equivalent power, respectively.

$$D^* = \frac{\sqrt{A}}{NEP} \left[\frac{m\sqrt{Hz}}{W} \right]$$

$$NEP(noise\ equivalent\ power) = \frac{noise\ [\frac{V}{\sqrt{Hz}}]}{Responsivity[\frac{V}{W}]}$$

For device presented in Fig. 2a:

$$NEP = \frac{30 \left[\frac{nV}{\sqrt{Hz}} \right]}{11.344 \left[\frac{mV}{W} \right]} = 2.65 \times 10^{-6} \left[\frac{W}{\sqrt{Hz}} \right]$$

$$D^* = \frac{\sqrt{0.424 \,\mu m^2}}{2.645 \times 10^{-6} \left[\frac{W}{\sqrt{Hz}}\right]} = 0.246 \left[\frac{m\sqrt{Hz}}{W}\right]$$

Similarly, in an ideal device with the noise solely limited by Johnson-Nyquist noise in the antenna itself, the NEP would be 11.9×10^{-8} W/Hz^{1/2}, and D^* would be 5.47 m Hz^{1/2}/W.

8. Supplementary figures:

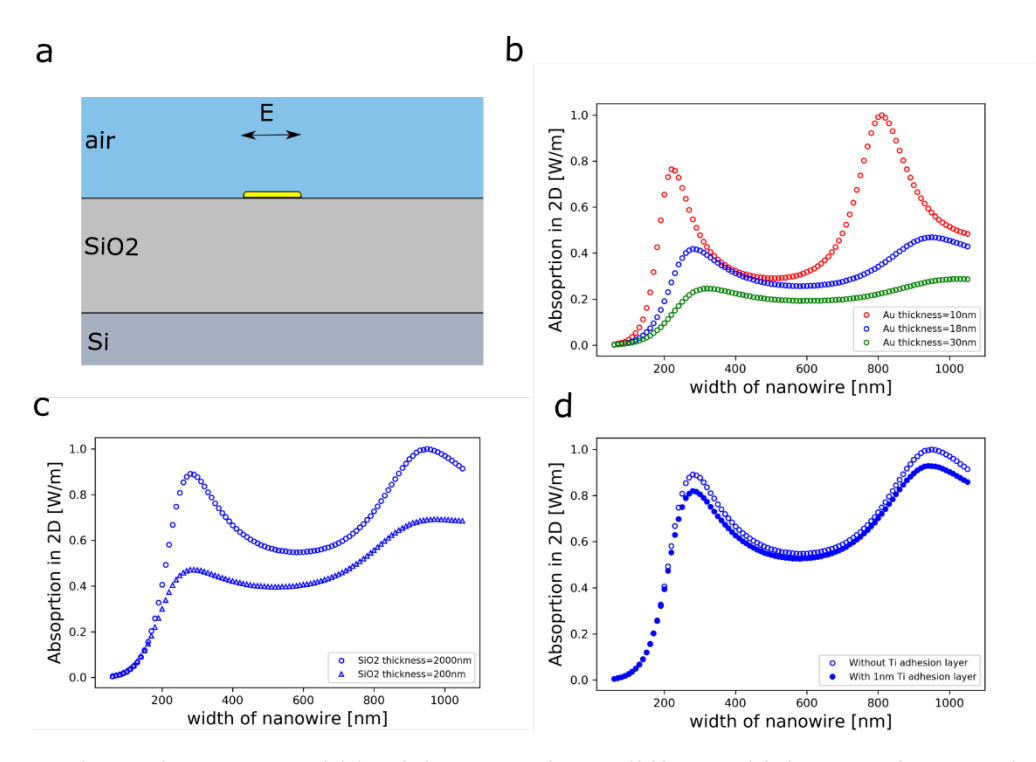


Figure S1. Absorption *versus* width of the nanowire at different thicknesses for Au, SiO_2 , and with and without adhesion laser. a) Absorption plots when SiO_2 thickness is fixed at 2 μ m and Au thickness changes. b) Absorption plots when Au thickness is fixed at 18 nm and SiO_2

thickness changes. c) Absorption plots when Au thickness is 18 nm and SiO_2 thickness is $2 \mu m$ with and without 1 nm Ti as an adhesion layer. All plots are normalized and the emphasis is on the relative absorption behavior.

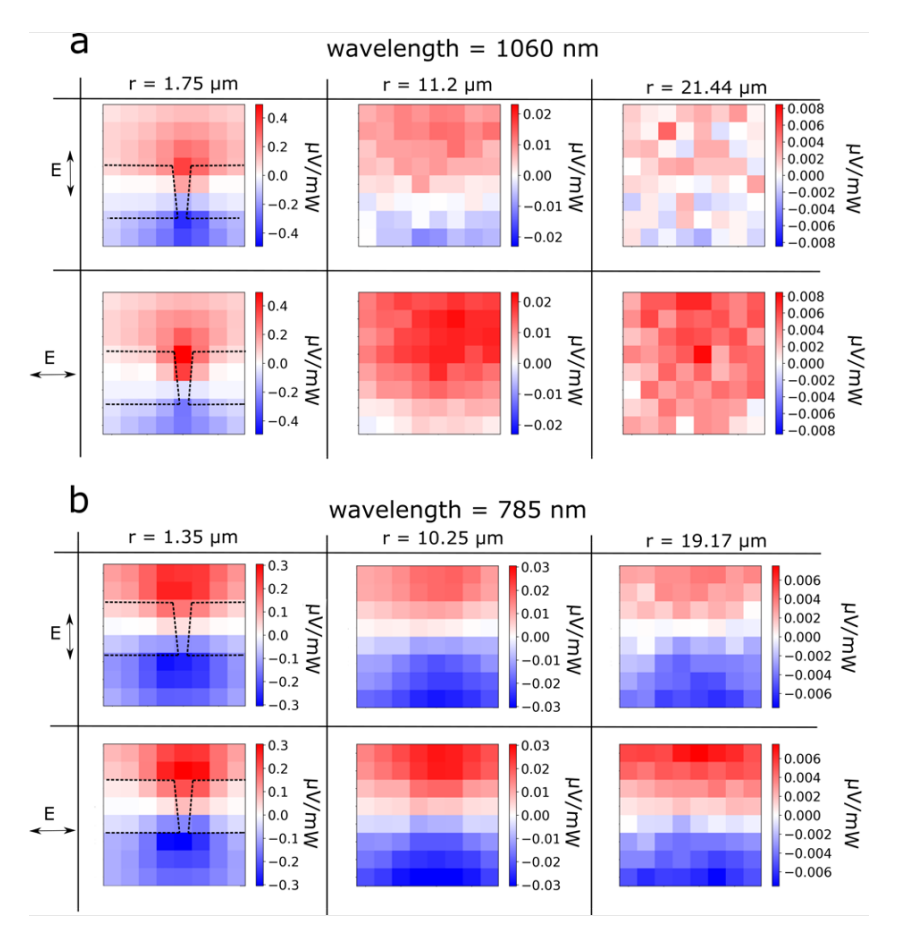


Figure S2. PTE map result for a device designed to detect 1060 nm efficiently at two wavelengths of 785 nm and 1060 nm. a) PTE map at different polarization and different laser sizes when a 1060 nm CW laser is used as the heat source. When the laser is expanded, the signal is dominated by the nanowire's active polarization side at transverse polarization. b) PTE results of the same device when a 785 nm laser is used as a heat source. When the laser is expanded, neither of the sides is dominant. This proves that each simple structured photodetector can be optimized for each wavelength.

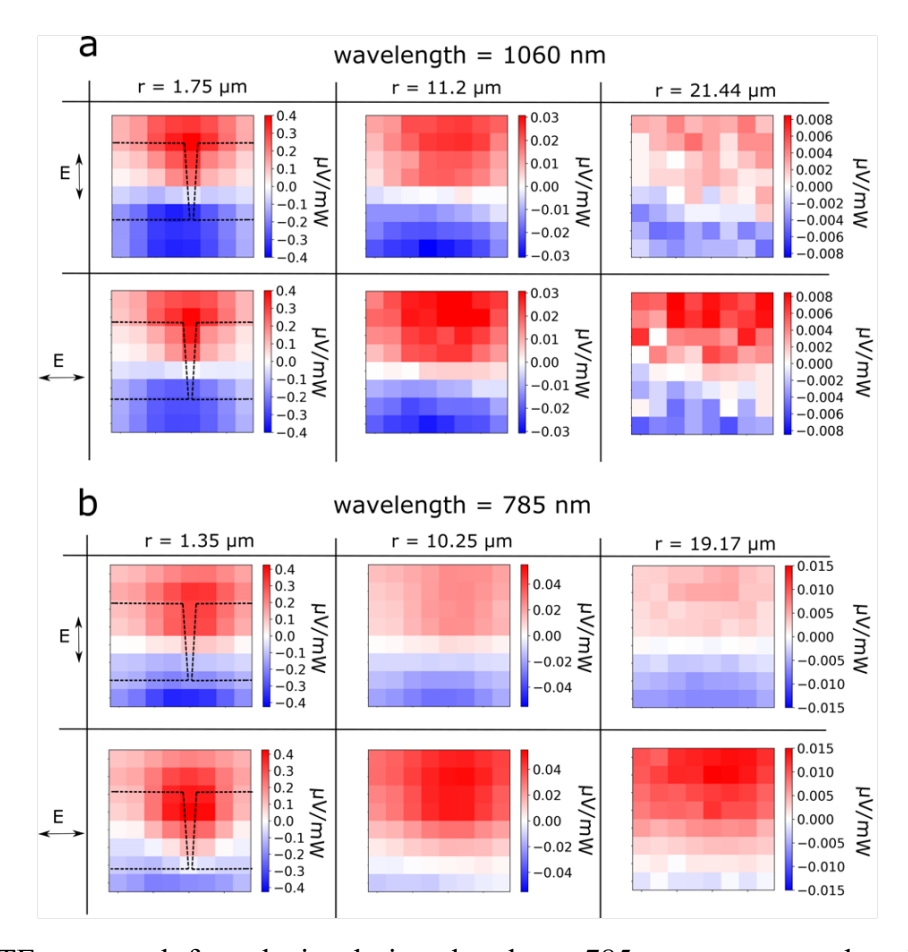


Figure S3. PTE map result for a device designed to detect 785 nm at two wavelengths of 785 nm and 1060 nm. a) PTE map at different polarization and different laser sizes when a 1060 nm CW laser is used as the heat source. When the laser is expanded, neither of the sides is dominant. b) PTE results of the same device when a 785 nm laser is used as a heat source. When the laser is expanded, the signal is dominated by the nanowire's active polarization side at transverse polarization. This proves that each simple structured photodetector is optimized for each wavelength.

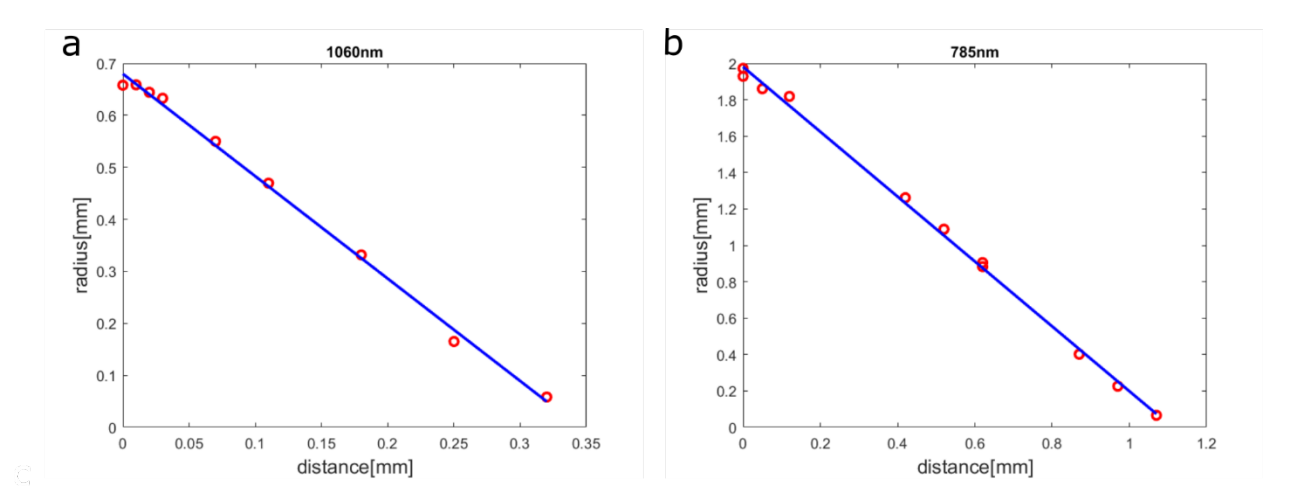


Figure S4. Knife-edge measurement results for two CW lasers used in the experiment. a) knife-edge measurement of 1060 nm CW laser. b) knife-edge measurement of 785 nm CW laser. The blue lines show the linear fit to the experimental data.

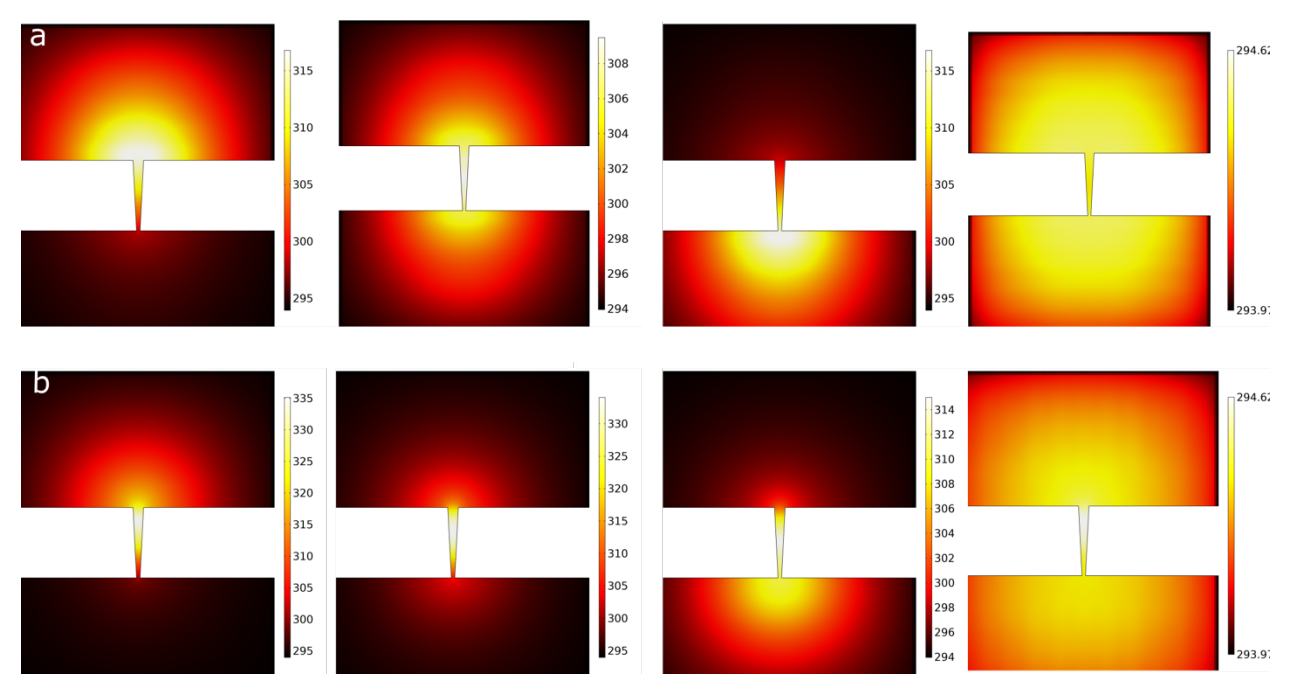


Figure S5. Temperature profiles of the device when using different laser positions and polarizations for the 1060 nm detector shown in Fig. 2a. a) When a longitudinal polarized laser is used. The laser is positioned on the top, middle, and bottom of the nanowire, respectively from

left to right. The rightest plot shows the temperature profile when the laser is expanded with diameters of 43 µm. For the expanded simulation, a plane wave with the same intensity as the expanded Gaussian beam is used as the optical source in simulations. b) the same results when a transversely polarized laser is used. All the temperature values are in Kelvin. The laser wavelength is 1060 nm in all the results. These results show that the plasmons increase the absorptions when transverse polarized light is used. When the laser is expanded, the temperature goes higher in the tapered nanowire when transverse polarization is used. This proves the polarization dependency of these photodetectors.

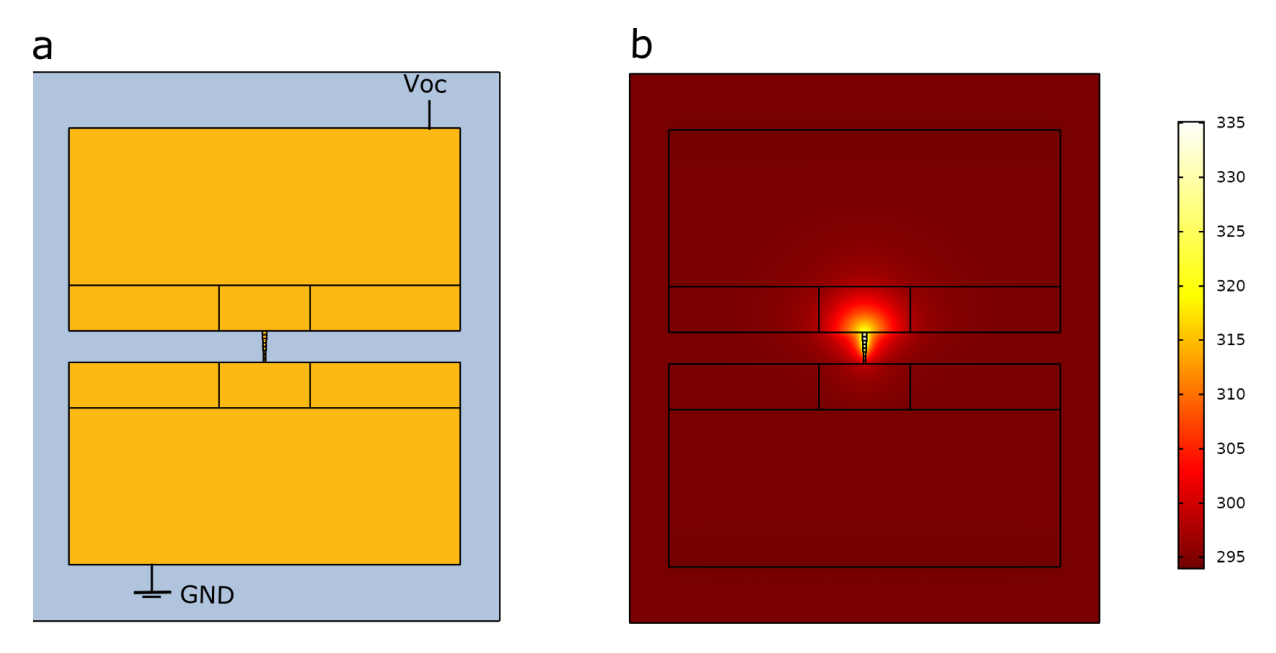


Figure S6. Simulation structure in Joule Heating simulations. a) the electrical boundary conditions, as well as the geometry, is shown. One side of the device is grounded, and the open circuit voltage is probed from the other end. b) temperature profile of the device. The temperature is imported from electromagnetic and heat transfer simulations that their results are presented in Fig. S5. The temperature unit is in Kelvin.

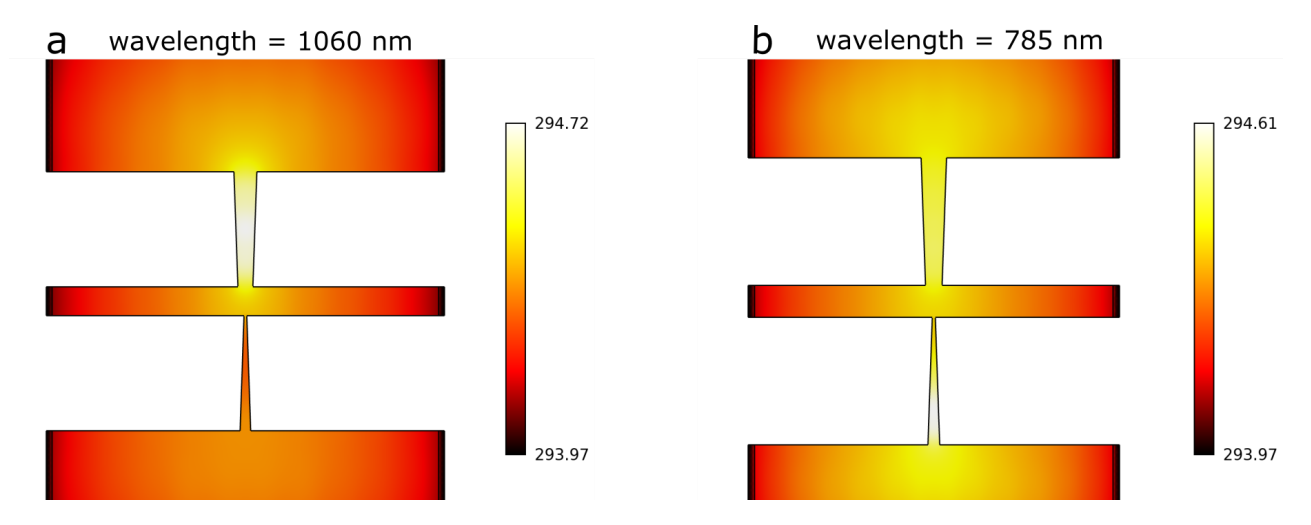


Figure S7. Simulation results of the temperature profile for the double wavelength photodetector presented in Fig. 3. a) 1060 nm plane wave with transverse polarization and with the same intensity and power as the expanded laser with a diameter of 43 μm is applied to the geometry. b) 785 nm plane wave with transverse polarization and with the same intensity and power of the expanded laser with a diameter of 56.2 μm is applied to the geometry. The temperature values are in Kelvin. Diameter of the expanded laser is the same as experimental results in Fig. 3.

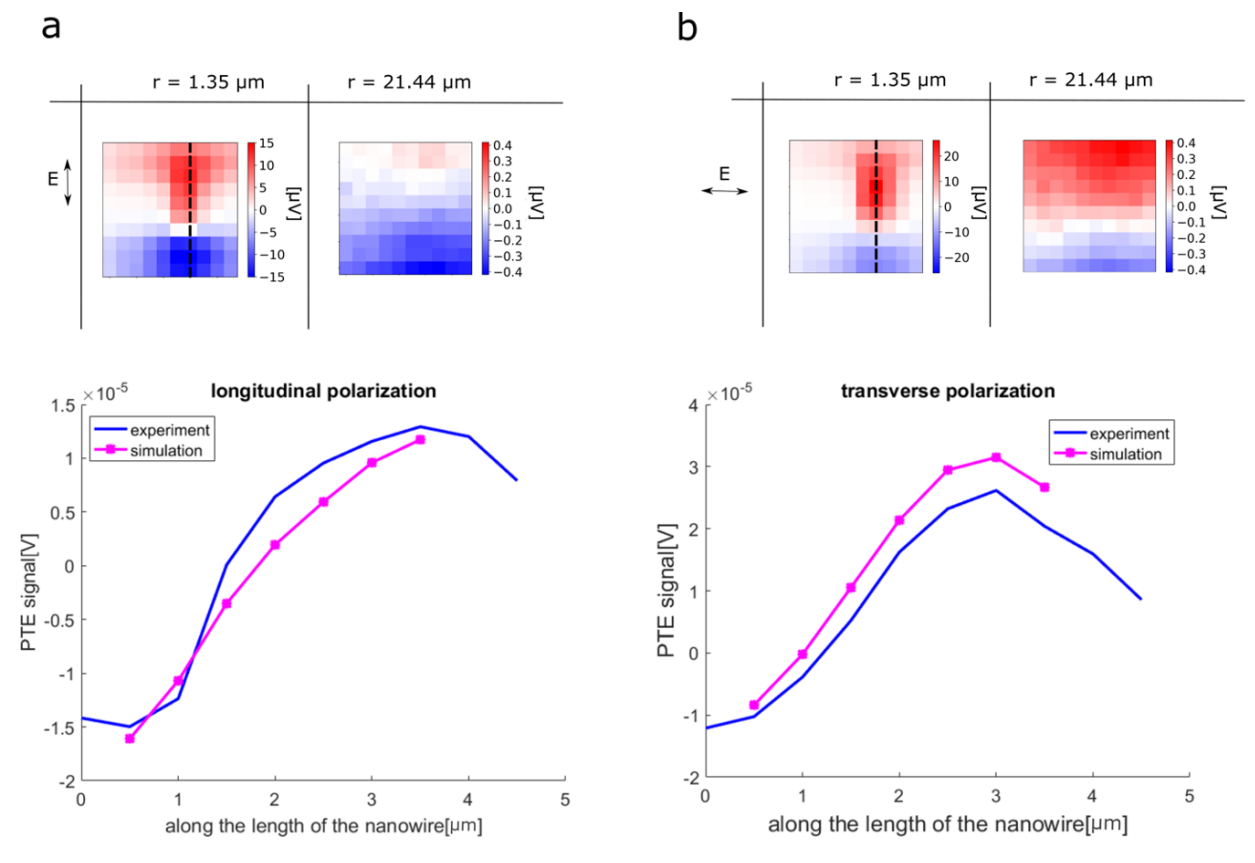


Figure S8. The simulation fit results for the Seebeck map of a single tapered nanowire photodetector. a) shows the results for longitudinally polarized laser. Focused laser and expanded laser results are shown on the top. The cut-through PTE signal from the dashed line on the focused PTE map is plotted on the bottom. The expanded signal from the middle of the device is considered to find the first fit parameters. The simulation results based on the calculated fit parameters are plotted in the bottom in pink for comparison with the experiment. The temperature profile for each of the dots in the pink plot is first calculated in COMSOL, then fit parameters, as well as calculated temperature, are used to simulate photovoltage for each spot location. b) shows the same results for the transversely polarized laser.

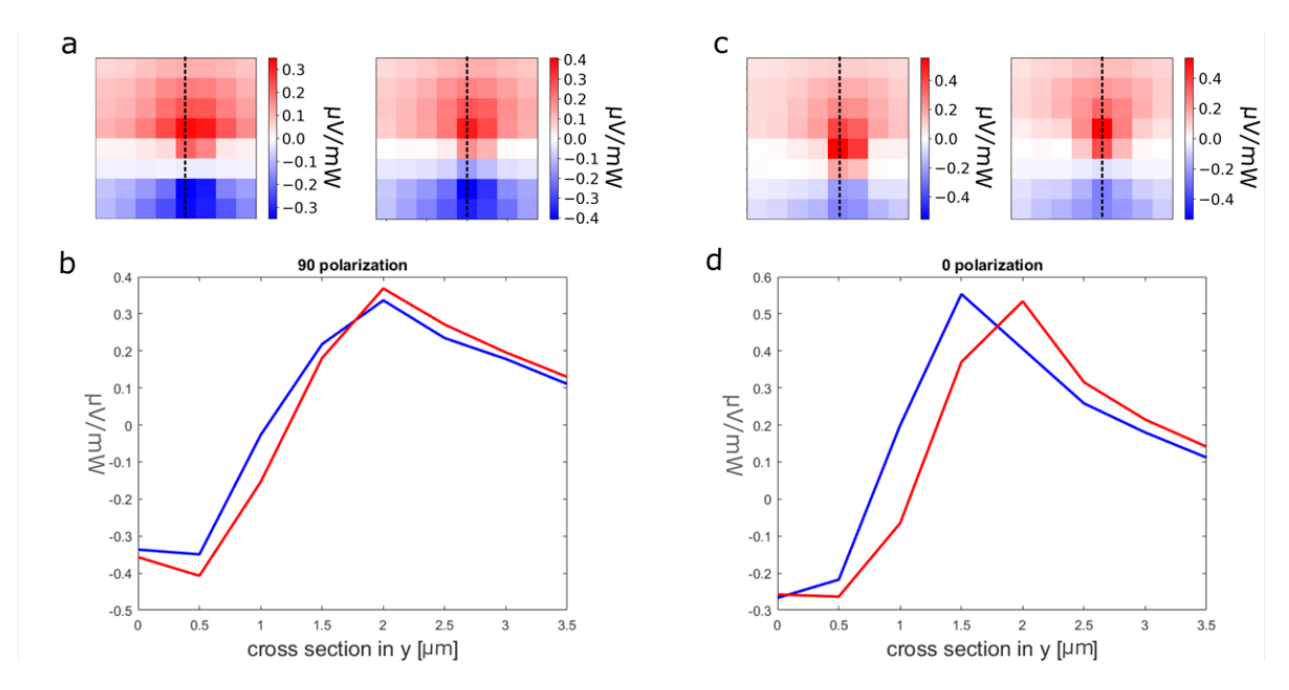


Figure S9. These plots show that when the PTE map measurement window is shifted for $0.3~\mu m$ in x and y, the cut-through plot can change. a) two consecutive measurements at transverse polarization when the laser is focused. The second measurement window is shifted by $0.3~\mu m$ in x and $0.3~\mu m$ in the y-direction. b) cut-through from the dotted line on PTE maps in Fig. S5a. c and d) the same measurements in transverse polarization.

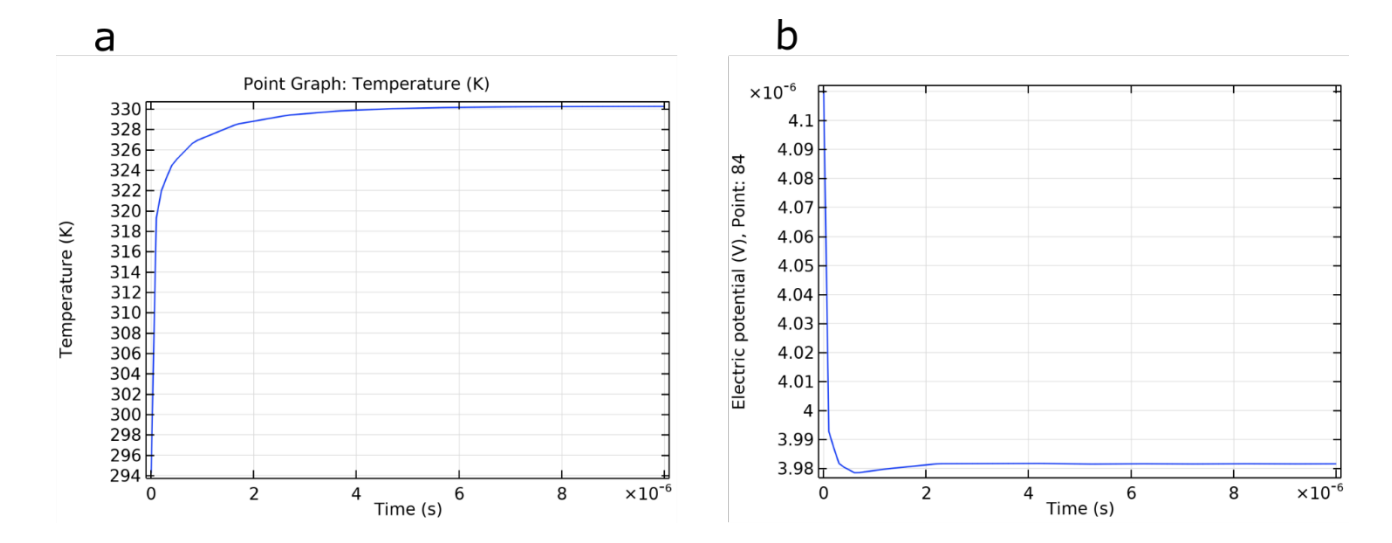


Figure S10. Time dependent simulations. a) Time dependent thermal simulation that shows stationary behavior at \sim 10 μ s. b) Time dependent PTE signal simulation that shows stationary behavior at \sim 8 μ s.

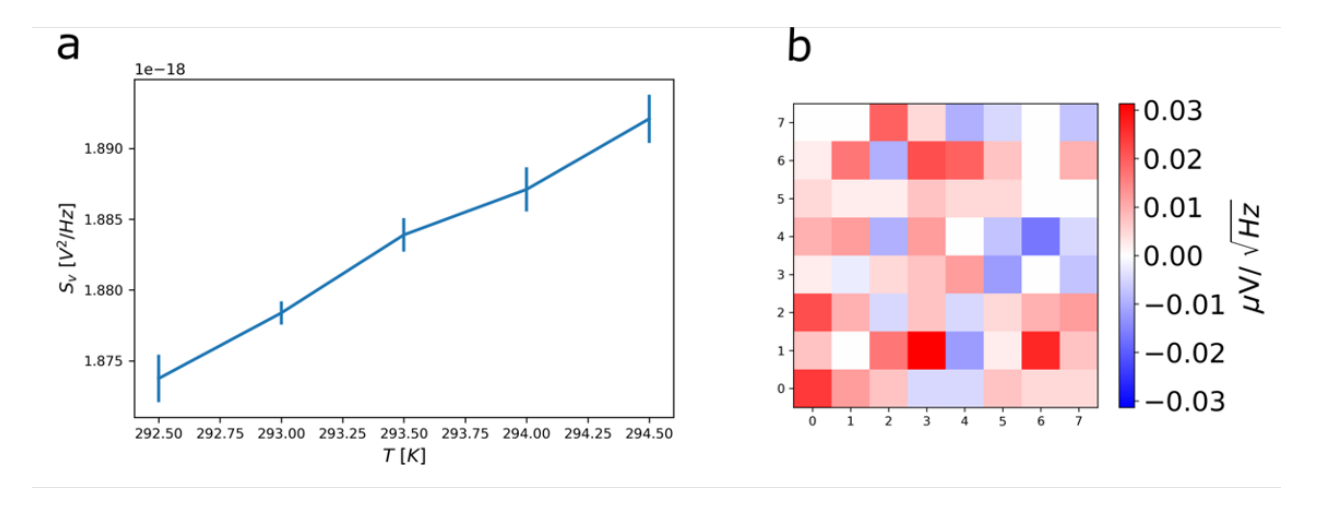


Figure S11. Noise measurement. a) Thermal noise measurement of a device at five points around the room T. The thermal noise is measured 15 times at each temperature. The vertical lines define the standard deviation of the measurements. b) PTE map of the device when laser is off.

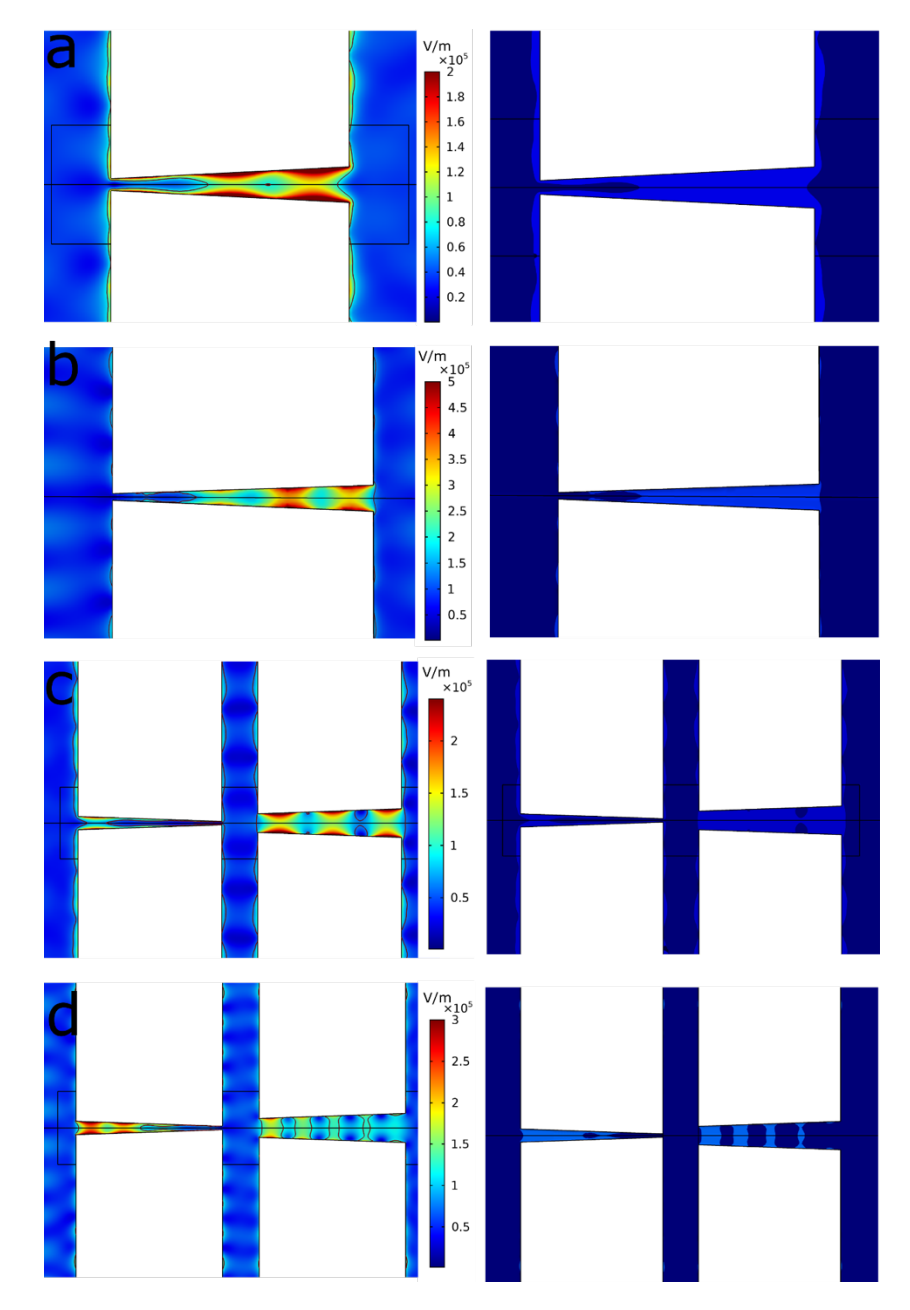


Figure S12. Effective area simulation of different photodetectors. The right column in each figure shows the total electric field plots overlapped with the effective area boundaries. The right column shows the effective area clearly. The light blue areas on the right figures show the effective area and the dark blue is outside of effective area. a) Field enhancement and the effective area results for a detector designed for 1060 nm wavelength (Fig. 2a) at 1060 nm incident wavelength with transverse polarization. b) Field enhancement and the effective area

results for a detector designed for 785 nm wavelength (Fig. 2c) at 785 nm incident wavelength with transverse polarization. c) Field enhancement and effective area results for the photodetector presented in Fig. 3 at 1060 nm. d) Field enhancement and effective area results for the photodetector presented in Fig. 3 at 785 nm.

9. SI references:

- S1. Cattani, M.; Salvadori, M. C.; Vaz, A. R.; Teixerira, F. S. Thermoelectric Power in Very Thin Film Thermocouples: Quantum Size Effect. J. Appl. Phys. **2006**, *100*, 114905.
- S2. Ho, C. Y.; Bogaard, R. H.; Chi, T. C.; Havill, T. N.; James, H. M.; Thermoelectric Power of Selected Metals and Binary Alloy Systems. Thermochimica Acta **1993**, *218*, 29-56.
- S3. Lin, F.; Leonard, W. F. Thermoelectric Power of Thin Gold Films. J. Appl. Phys. **1971**, *42*, 3634–3639.
- S4. Fuchs, K.; Wills. H. H. The Conductivity of Thin Metallic Films According to the Electron Theory of Metals. Mathematical Proceedings of the Cambridge Philosophical Society **1938**, *34*(1), 100-108.
- S5. Johnson, P. B.; Christy, R. W. Optical Constants of the Noble Metals. Phys. Rev. B **1972**, *6*(12), 4370-4379.
- S6. Aspnes, D. E.; Studna, A. A. Dielectric Functions and Optical Parameters of Si, Ge, GaP, GaAs, GaSb, InP, InAs, and InSb from 1.5 to 6.0 eV. Phys. Rev. B **1983**, *27*(2), 985-1009.
- S7. Malitson I. H. Interspecimen Comparison of the Refractive Index of Fused Silica. J. Opt. Soc. Am. **1965**, *55*(10), 1205-1209.
- S8. Gonzalez-Cardel, M.; Arguijo, P.; Diaz-Uribe, R. Gaussian Beam Radius Measurement with a Knife-Edge: A Polynomial Approximation to the Inverse Error Function. Appl. Optics **2013**, Vol. *52*, 3849-3855.

S9. Alda, J.; Fumeaux, C.; Codreanu, I.; Schaefer, J.A.; Boreman, G.D. Deconvolution Method for Two Dimensional Spatial-Response Mapping of Lithographic Infrared Antennas. Appl Opt. **1999**, *38*, 3993-4000.